Macromolecular Architecture in Eukaryotic Cells Visualized by Cryoelectron Tomography

Ohad Medalia, Igor Weber, Achilleas S. Frangakis, Daniela Nicastro, Günther Gerisch, Wolfgang Baumeister*

Electron tomography of vitrified cells is a noninvasive three-dimensional imaging technique that opens up new vistas for exploring the supramolecular organization of the cytoplasm. We applied this technique to *Dictyostelium* cells, focusing on the actin cytoskeleton. In actin networks reconstructed without prior removal of membranes or extraction of soluble proteins, the cross-linking of individual microfilaments, their branching angles, and membrane attachment sites can be analyzed. At a resolution of 5 to 6 nanometers, single macromolecules with distinct shapes, such as the 26*S* proteasome, can be identified in an unperturbed cellular environment.

Visualizing the three-dimensional (3D) organization of eukaryotic cells, with their dynamic organelles, cytoskeletal structures, and molecular machines in an unperturbed context, requires a noninvasive, high-resolution imaging technique combined with a method of arresting cells in their momentary state of function. Electron tomography (ET) has a unique potential for this purpose (*1*, *2*). Conventional electron microscopic images are essentially 2D projections of the object: Features are superimposed upon one another in the direction of the electron beam. Tomographic techniques, in contrast, acquire projections of the object as viewed from different directions and then merge them computationally into a 3D reconstruction, the tomogram. In ET this is done by tilting the specimen holder incrementally around an axis perpendicular to the electron beam.

Although ET is not a new concept [see, e.g. (*3*)], formidable experimental problems stood in the way of practical applications for more than three decades. Basically, there are two conflicting requirements, which are difficult to reconcile. On the one hand, resolution and quality of a tomogram are directly dependent on spacing of the projections and on the angular range covered. Therefore, data must be collected over a tilt range as wide as possible, with increments as small as possible. On the other hand, the exposure to the electron beam must be minimized to prevent radiation damage (*4*, *5*). The development of elaborate automated data-acquisition procedures enabled us to reduce beam exposure dramatically (*6*, *7*) and to take advantage of the principle of dose fractionation (*8*, *9*). With these improvements, ET could be applied to radiation-sensitive specimens, such as biological materials embedded in amorphous ice (*10*–*12*). Vitrification by rapid freezing ensured close-to-life preservation of cellular structures, avoiding the risk of artifacts associated with chemical fixation, staining, or dehydration.

Specimen thickness is a major limitation in ET. When it exceeds the mean free path of electrons, multiple inelastic scattering begins to degrade the quality of images substantially, despite the use of higher voltages (300 to 400 keV) and energy filters to temper these effects (*13*). In consequence, samples thicker than 1 μm cannot be studied in toto, but must be (cryo)sectioned before tomographic analysis. Many prokaryotic cells are small enough to be examined by cryo-ET without the need of sectioning, and some eukaryotic cells can be grown flat enough to apply cryo-ET at least locally in a noninvasive manner. Here we apply this method to the highly motile cells of *Dictyostelium discoideum*. A prerequisite for studying intact eukaryotic cells by cryo-ET is their ability to spread on electron microscope grids (see supporting online methods) (*14*). *Dictyostelium* cells moving on a copper grid coated by a plain carbon film are shown in Movie S1. These cells assume their normal shape, migrate, and even divide as on a glass surface. The grids with the cells enclosed in a thin aqueous layer are plunge-frozen to achieve vitrification.

Zooming into intact vitrified cells. The cellular regions that we examined by cryo-ET varied between 300 and 600 nm in thickness. Two-dimensional projection images of such regions, obtained by conventional cryoelectron microscopy (cryo-EM), are hard to interpret because of the superposition problem noted above. Only membranes and other features that are continuous through most of the volume are clearly visible (Fig. 1A). Because in computing a tomogram the information from many statistically noisy projections is combined, the signal-to-noise ratio is significantly improved as compared with individual projections. Nevertheless, there is substantial residual noise because data sets need to be recorded under the constraint of a subcritical cumulative electron dose. But even without further "denoising" or averaging of segmented features, some structural elements are clearly visible in a tomogram displayed in the form of 60-nm-thick *x*-*y* slices along the *z* axis, in particular microfilaments and a population of high-density particles roughly 30 nm in size (Fig. 1, B to D). As an example of intracellular organelles that can be studied by cryo-ET in their native environment, we focus in Fig. 1, E and F, on the rough endoplasmic reticulum (ER). *Dictyostelium* cells have a profusely developed ER, which extends from the nucleus up to the inner face of the cortical actin layer (*15*). Figure 1E shows a series of *x*-*y* slices through a portion of the rough ER located within the peripheral region of a cell (framed white in Fig. 1A). The membrane is decorated with an array of globular complexes, which resemble 80*S* ribosomes in size (~27 nm) and shape (Fig. 1F). Their high contrast is consistent with a particle containing mostly RNA. We assume that the high-density particles in the cytoplasm, often nestled in the actin cytoskeleton, are also ribosomes. The interior of the ER is highly crowded, making it difficult to identify distinct features in this compartment.

Visualizing a macromolecular complex in situ: the 26*S* proteasome. The less-crowded environment in the cytoplasm allows one to search the tomograms interactively for complexes recognizable through their structural signature, i.e., their size and shape. A particularly striking example of a large protein complex residing in the cytoplasm is the 26*S* proteasome, the most downstream element of the ubiquitin pathway of protein degradation (*16*). This molecular machine of 2.5 MD has a characteristic elongated shape (45 nm in length) reminiscent of a "double dragon head" (*17*–*19*). When subtomograms containing this motif were extracted (Fig. 2A) and the slices containing this structure were summed, the resulting projection image (Fig. 2B) corresponded closely to an average derived from purified *Xenopus* 26*S* proteasomes (Fig. 2C). There are a few subtle differences in the region connecting the base and the lid of the 19*S* regulatory subcomplex, but this is known to be a weak and flexible linkage (*20*). Despite the relatively low resolution of the tomogram (~5 to 6 nm), the similarity with the 26*S* complex from *Xenopus* is striking and the identification is unambiguous.

Capturing unperturbed actin networks without removal of membranes. Cell motility, endocytosis, and cytokinesis rely on the

Max Planck Institute for Biochemistry, D-82152 Martinsried, Germany.

*To whom correspondence should be addressed. E-mail: baumeist@biochem.mpg.de

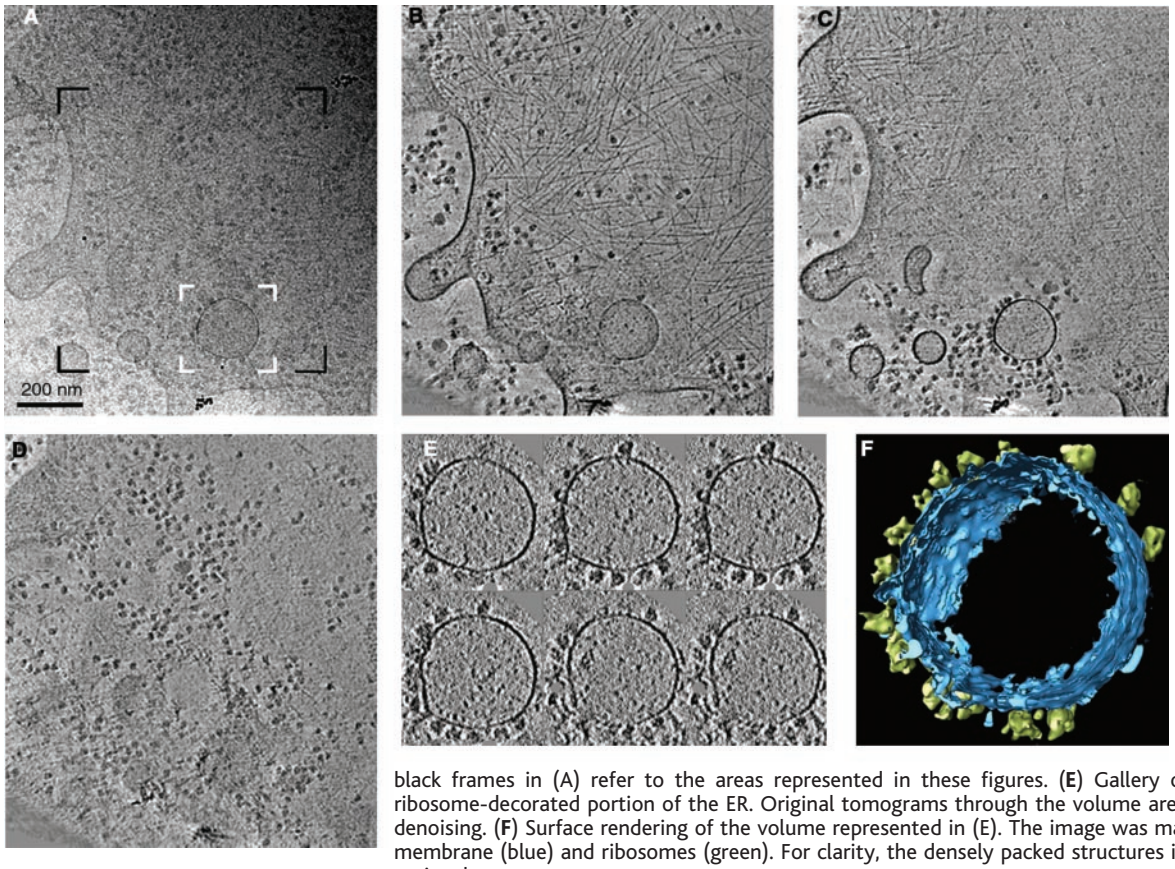

Fig. 1. Peripheral region of a vitrified *Dictyostelium* cell analyzed by cryo-ET. (**A**) Conventional transmission electron micrograph (2D projection) of the region used for recording a tilt series. Thickness of the cell in this region varied from 200 to 350 nm. (**B** to **D**) Series of successive tomographic *x-y* slices of 60-nm thickness from bottom to top of the substrate-attached region of the cell. In (B) and (C), portions of the plasma membrane that are perpendicular to the *x-y* plane can be recognized. In (B), the cortical actin network is viewed. Detailed images of the molecular complexes and vesicular structures are shown in (E) and in Fig. 3; white and black frames in (A) refer to the areas represented in these figures. (**E**) Gallery of *x-y* slices through a ribosome-decorated portion of the ER. Original tomograms through the volume are displayed without any denoising. (**F**) Surface rendering of the volume represented in (E). The image was manually segmented into membrane (blue) and ribosomes (green). For clarity, the densely packed structures in the lumen have been omitted.

spatially and temporally controlled assembly and disassembly of actin filaments. Light and electron microscopy have provided important insights into actin-filament organization and its changes in response to external signals. A variety of electron microscopic techniques have been used to study cytoskeletons; some are based on fixed and sectioned material, and others use detergent-extracted or mechanically unroofed cells (*21*–*24*). The cytoskeletons can be visualized by negative staining or by freeze-drying in conjunction with platinum replication (*21*). As recently shown, artifacts associated with freeze-drying can be avoided by direct observation of frozen cytoskeletons from detergent-extracted cells (*24*).

In the cell cortex, actin filaments are interconnected in various modes, forming networks anchored to the inner face of the plasma membrane. Polymerization and depolymerization, cross-linking, and branching of actin filaments are regulated by different proteins that act together in determining cell shape and motility (*25*–*27*). Actin organization in *Dictyostelium* cells is similar to that in neutrophils and other fast-moving animal cells, and many of the proteins identified in mammalian cells have homologs in *Dictyostelium* (*28*–*32*). These include the Arp2/3 complex and a filamin-like F-actin cross-linker (*33*, *34*).

In highly motile cells, like those of *Dictyostelium*, the actin filament system is reorganized within seconds (*35*). The structure of these networks in any part of the cell is transient and reflects their momentary role in cell motility, endocytosis, or mitotic cell division. Because of the dynamic nature of the actin cytoskeleton, it is essential to combine ET with cryotechniques, which allow one to vitrify the sample, avoiding perturbation of the delicate balance of regulatory proteins in this system.

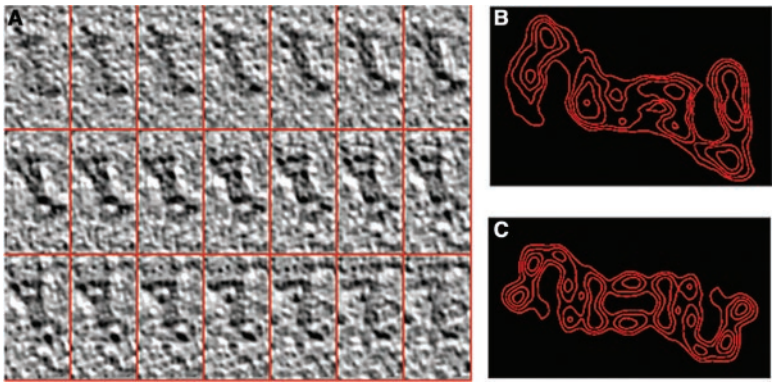

Fig. 2. Structure of a 26*S* proteasome as visualized in its cytoplasmic context. (**A**) *x-y* slices through the volume of the proteasome. (**B**) Density profile of a 2D projection of the volume represented in (A). (**C**) Reference image of the averaged 2D structure of a purified and negatively stained 26*S* proteasome from *Xenopus* oocytes (*44*).

Here, we report that cryo-ET allows visualization of the actin filament network without any pretreatment and in its native association with cellular membranes. Thus, two major risks are avoided. First, actin-binding proteins may rapidly dissociate from, or artificially bind to, the actin network during the treatment of cells with detergent. In both cases, the connections between actin filaments and thus the structure of the network will be altered. Second, distortions of the network caused by its detachment from membranes are prevented and, by the same token, the sites of membrane attachment can be studied.

The cortical region of the cell shown in Fig. 1, A to D, is dominated by the network of actin filaments, with ribosomes and other

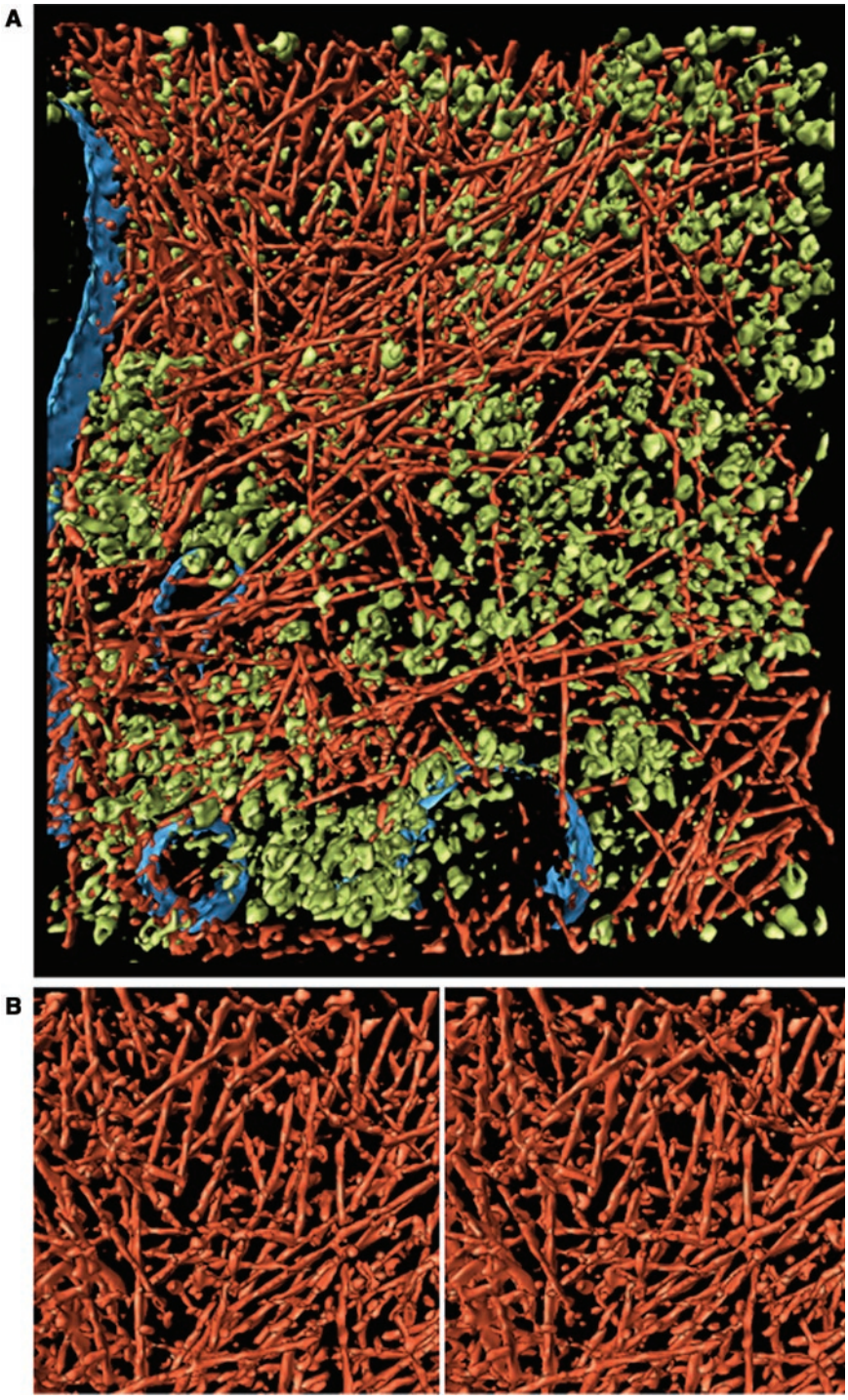

Fig. 3. Visualization of actin network, membranes, and cytoplasmic macromolecular complexes. (**A**) A volume of 815 nm by 870 nm by 97 nm, corresponding to the area of Fig. 1A framed in black, was subjected to surface rendering. Colors were subjectively attributed to linear elements to mark the actin filaments (reddish); other macromolecular complexes, mostly ribosomes (green); and membranes (blue). (**B**) Stereo image of an actin layer taken from the upper left portion of (A) reveals a crowded network of branched and crosslinked filaments.

macromolecular complexes in between. This becomes particularly clear after surface rendering of the tomogram (Fig. 3A). Figure 3B shows an enlargement of a subvolume crowded with actin filaments and displays the network in stereo. From this network and from similar ones, we have extracted X-, Y-, and T-shaped junctions between the actin filaments; 12 of them are displayed in the gallery shown in Fig. 4. Among these examples, branching angles vary between 40° and 90°. Some branches show the arm linked to an actin filament out of plane, as illustrated in Fig. 4A (top). A special feature of some branches is visible in Fig. 4B: The side arms are sharply bent close to their site of attachment. This is presumably caused by an actin-binding protein that links one end of a filament to the side of another one. The putative linker protein sticks out of a filament at a wide angle. Cross-linking of actin filaments occurs often at a 90° angle (Fig. 4C).

Figure 5A shows a series of *x*-*y* slices from a tomogram of another cortical region with actin filaments predominantly arranged in parallel; for clarity, the sections were denoised. Although this tomogram is of inferior quality owing to the greater local thickness of the cell (~600 nm), the arrangement of actin filaments is clearly visible. Individual filaments can be traced over a length of 400 to 500 nm, which is twice the reported average length (*36*). Such parallel arrangements are typically generated and stabilized by bundling proteins forming serial bridges along the individual filaments. Indeed, at many locations such bridges are discernible in Fig. 5B; two of them are displayed in Fig. 5C.

Because in cryo-ET the integrity of the cellular membranes is maintained, we were able to depict binding sites of actin filaments on the plasma membrane. Figure 6A shows a cortical actin-filament network locally connected to the plasma membrane, and in Fig. 6, B and C, surface-rendered actin filaments are presented that appear to be kinked close to the membrane surface. These images indicate that actin filaments are capable of end binding to the plasma membrane through a connecting element that forms the kink. This element might be an adaptor protein or the cytoplasmic domain of an actin-binding transmembrane protein.

In summary, cryo-ET of peripheral regions in *Dictyostelium* L cells depicted two different types of actin-filament arrays: almost isotropic networks (Fig. 3) and parallel arrangements of actin filaments that are tied together by bundling proteins (Fig. 5). Within the actin networks, we have found a broad distribution of branching angles and different types of cross-linkages (Fig. 4). These observations are consistent with the presence in eukaryotic cells of a large variety of actin-cross-linking and actin-branching proteins that connect actin filaments to each other at angles varying from 0° (parallel bundling) to 180° (antiparallel bundling). Groups of conserved branching and cross-linking proteins include the Arp2/3 complex, which is characterized by a 70° angle of branching (*37*, *38*), and the filamin family (with filamin A as a prototype), which has a preference for orthogonal crosslinkage of actin filaments (*23*, *34*). An advantage of cryo-ET is that branching angles can be determined precisely from the 3D maps. The quantitative analysis of network geometries will benefit from automated procedures, allowing the evaluation of large tomographic data sets.

Prospects of cryo-ET applied to cell biology. Cryo-ET has the potential to bridge the gap between cellular and molecular structural studies (*39*). By combining the power of 3D imaging with the close-to-life preservation achieved by vitrification, we have visualized macromolecular complexes and supramolecular structures inside intact eukaryotic cells. The tomograms of *Dictyostelium* cells contain an imposing amount of information, even at the present resolution of 5 to 6 nm. Essentially, they are 3D images of the cell's entire proteome, and they represent the network of macromolecular interactions that provides the basis for coordinated cellular activities. Exploitation of this information is confronted with a number of problems. Despite advanced image-acquisition procedures and the application of denoising techniques, cryoelectron tomograms still suffer from substantial residual noise and distortions because of missing data. Moreover, the cytoplasm and organelles are crowded with macromolecules, which often makes it impossible to perform segmentation and feature extraction on the basis of visual inspection of the tomograms, except for large and continuous structures such as membranes and filaments.

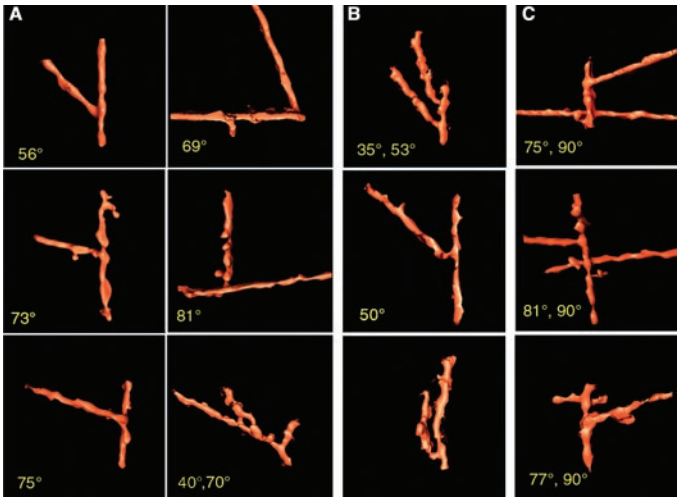

Fig. 4. Branches and crosslinks of actin filaments. These examples were chosen from the cortical regions of cells as in Fig. 3. The branching angles as displayed in 2D were extracted and maximized in 3D. (**A**) Compilation of branchings with different angles. (**B**) Examples characterized by a kink that changes the angle close to the branching site. (**C**) Cross-linkages between filaments in addition to branches.

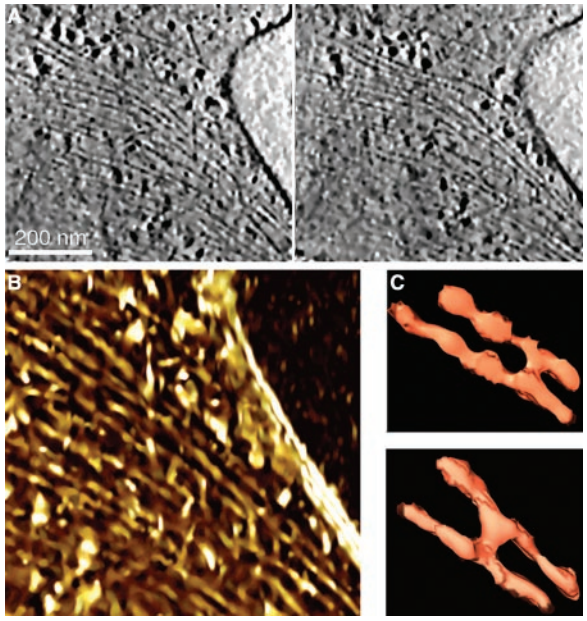

Fig. 5. Bundles of actin filaments in the cell cortex. (**A**) Two denoised *x-y* slices of 10-nm thickness through the cortical region of a cell, sampled at 490 to 510 nm above the substrate. (**B**) A volume-rendered portion of the region depicted in (A) showing bridges between filaments and lateral connections of filaments to the membrane. (**C**) Representative bridges between actin filaments extracted from (B).

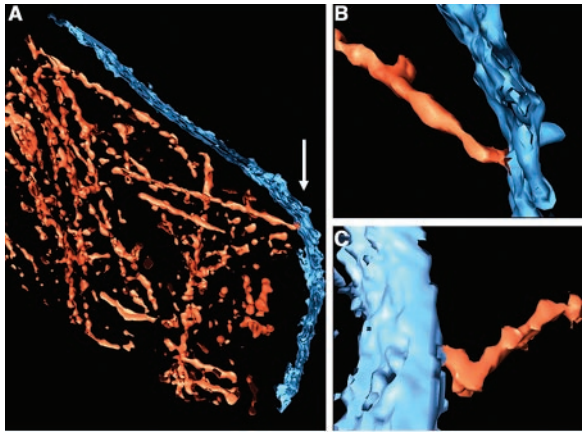

Fig. 6. End binding of actin filaments to the plasma membrane. (**A**) Cortical region of 500 nm by 300 nm by 20 nm showing membrane-associated actin filaments presented as in Fig. 3. The arrow points to the site of actin-membrane interaction shown in (B) at higher magnification. (**B** and **C**) High-magnification image of cortical regions, depicting kinklike structures close to filament-membrane interaction sites. Kink angles were not maximized, and the membrane in (C) was not perpendicular to the actin filament. (B) and (C) were taken from different cortical regions.

In applying cryo-ET to dynamic cytoskeletal arrangements, a major goal will be to assign the types of branches and cross-linkages to specific linker proteins. This might be accomplished by different routes. The structural analysis of mutants that miss specific actin–cross-linking proteins or that lack combinations of these proteins will help to identify the individual contributions of major players in the dynamic organization of actin networks. Another possibility is the combination of cryo-ET with the labeling of specific proteins by microinjected gold-conjugated antibodies. Finally, at higher resolution it will be possible to detect and identify cross-linking proteins by a template-matching approach, as currently explored for larger cytoplasmic protein complexes (*42*). Because prospects for a significant improvement in resolution to 1.5 to 2.0 nm are good (*43*), it will ultimately be possible to generate pseudoatomic maps of large supramolecular assemblies or even whole organelles by docking high-resolution structures of molecular components into cellular tomograms.

References and Notes

1. W. Baumeister, R. Grimm, J. Walz, *Trends Cell Biol.* **9**, 81 (1999).
2. B. F. McEwen, J. Frank, *Curr. Opin. Neurobiol.* **11**, 594 (2001).
3. R. G. Hart, *Science* **159**, 1464 (1968).
4. Reviewed in A. J. Koster *et al.*, *J. Struct. Biol.* **120**, 276 (1997).
5. Reviewed in B. F. McEwen, M. Marko, *J. Histochem. Cytochem.* **49**, 553 (2001).
6. K. Dierksen, D. Typke, R. Hegerl, A. J. Koster, W. Baumeister, *Ultramicroscopy* **40**, 71 (1992).
7. K. Dierksen, D. Typke, R. Hegerl, W. Baumeister, *Ultramicroscopy* **49**, 109 (1993).
8. R. Hegerl, W. Hoppe, *Z. Naturforsch. Sect. A Phys. Sci.* **31**, 1717 (1976).
9. B. F. McEwen, K. H. Downing, R. M. Glaeser, *Ultramicroscopy* **60**, 357 (1995).
10. R. Grimm *et al.*, *Biophys. J.* **72**, 482 (1997).
11. R. Grimm *et al.*, *Biophys. J.* **74**, 1031 (1998).
12. D. Nicastro, A. S. Frangakis, D. Typke, W. Baumeister, *J. Struct. Biol.* **129**, 48 (2000).
13. R. Grimm, A. J. Koster, U. Ziese, D. Typke, W. Baumeister, *J. Microsc.* **183**, 60 (1996).
14. Materials and methods are available as supporting material on *Science* Online.
15. A. Muller-Taubenberger *et al.*, *EMBO J.* **20**, 6772 (2001).
16. D. Voges, P. Zwickl, W. Baumeister, *Annu. Rev. Biochem.* **68**, 1015 (1999).
17. J. M. Peters, Z. Cejka, J. R. Harris, J. A. Kleinschmidt, W. Baumeister, *J. Mol. Biol.* **234**, 932 (1993).
18. M. Rechsteiner, L. Hoffman, W. Dubiel, *J. Biol. Chem.* **268**, 6065 (1993).
19. H. Holzl *et al.*, *J. Cell Biol.* **150**, 119 (2000).
20. M. H. Glickman *et al.*, *Cell* **94**, 615 (1998).
21. J. E. Heuser, M. W. Kirschner, *J. Cell Biol.* **86**, 212 (1980).
22. T. M. Svitkina, A. B. Verkhovsky, K. M. McQuade, G. G. Borisy, *J. Cell Biol.* **139**, 397 (1997).
23. L. A. Flanagan *et al.*, *J. Cell Biol.* **155**, 511 (2001).
24. G. P. Resch, K. N. Goldie, A. Krebs, A. Hoenger, J. V. Small, *J. Cell Sci.* **115**, 1877 (2002).
25. Reviewed in J. E. Bear, M. Krause, F. B. Gertler, *Curr. Opin. Cell Biol.* **13**, 158 (2001).
26. Reviewed in D. Pantaloni, C. Le Clainche, M. F. Carlier, *Science* **292**, 1502 (2001).
27. Reviewed in J. V. Small, T. Stradal, E. Vignal, K. Rottner, *Trends Cell Biol.* **12**, 112 (2002).
28. C. Hug *et al.*, *Cell* **81**, 591 (1995).
29. M. Haugwitz, A. A. Noegel, J. Karakesisoglou, M. Schleicher, *Cell* **79**, 303 (1994).
30. J. Niewöhner, I. Weber, M. Maniak, A. Muller-Taubenberger, G. Gerisch, *J. Cell Biol.* **138**, 349 (1997).
31. M. Tsujioka, L. M. Machesky, S. L. Cole, K. Yahata, K. Inouye, *Curr. Biol.* **9**, 389 (1999).
32. E. L. de Hostos, *Trends Cell Biol.* **9**, 345 (1999).
33. R. Insall *et al.*, *Cell Motil. Cytoskel.* **50**, 115 (2001).
34. T. P. Stossel *et al.*, *Nature Rev. Mol. Cell. Biol.* **2**, 138 (2001).
35. E. Lee, K. Pang, D. A. Knecht, *Biochim. Biophys. Acta* **1525**, 217 (2001).
36. J. L. Podolski, T. L. Steck, *J. Biol. Chem.* **265**, 1312 (1990).
37. R. D. Mullins, J. A. Heuser, T. D. Pollard, *Proc. Natl. Acad. Sci. U.S.A.* **95**, 6181 (1998).
38. H. N. Higgs, T. D. Pollard, *Annu. Rev. Biochem.* **70**, 649 (2001).
39. M. Schliwa, *Nature Rev. Mol. Cell. Biol.* **3**, 291 (2002).
40. Reviewed in R. Grünewald, O. Medalia, A. Gross, A. C. Steven, W. Baumeister, *Biophys. Chem.*, in press.
41. J. Böhm *et al.*, *Proc. Natl. Acad. Sci. U.S.A.* **97**, 14245 (2000).
42. A. S. Frangakis *et al.*, *Proc. Natl. Acad. Sci. U.S.A.* **99**, 14153 (2002).
43. J. M. Plitzko *et al.*, *Trends Biotechnol.* **20**, S40 (2002).
44. J. Walz *et al.*, *J. Struct. Biol.* **121**, 19 (1998).

45. O.M. thanks the European Commission for a Marie Curie fellowship. I.W. was supported by a grant from the Deutsche Forschungsgemeinschaft (SFB 266 to G.G.). We thank J. Köhler for the movie and A. C. Steven for critical reading of the manuscript.

Supporting Online Material

www.sciencemag.org/cgi/content/full/298/5596/1209/DC1
Materials and Methods
Movie S1

16 July 2002; accepted 9 September 2002

Superconductivity in Dense Lithium

Viktor V. Struzhkin,[1]* Mikhail I. Eremets,[2] Wei Gan,[1,3] Ho-kwang Mao,[1] Russell J. Hemley[1]

Superconductivity in compressed lithium is observed by magnetic susceptibility and electrical resistivity measurements. A superconducting critical temperature (T_c) is found ranging from 9 to 16 kelvin at 23 to 80 gigapascals. The pressure dependence of T_c suggests multiple phase transitions, consistent with theoretical predictions and reported x-ray diffraction results. The observed values for T_c are much lower than those theoretically predicted, indicating that more sophisticated theoretical treatments similar to those proposed for metallic hydrogen may be required to understand superconductivity in dense phases of lithium.

Lithium is considered the simplest metal: it is the lightest of the alkali metals, and under normal pressure-temperature conditions its properties are well described within a nearly free electron model. The two inner core electrons effectively shield the nucleus, inhibiting electron-ion attraction and leaving the outer electrons to move freely within the ion lattice. Because the valence electron is so delocalized, lithium is a metal with high conductivity and it assumes a highly symmetric body-centered cubic (bcc) structure. Recent studies show that under pressure, however, this simplicity changes radically. Theoretical predictions (*1*) suggest that lithium may undergo several structural transitions, possibly leading to a "paired-atom" phase with low symmetry and near-insulating properties. Though this prediction is the antithesis of the intuitive expectation that pressure favors high-symmetry crystal structures with metallic properties, recent x-ray diffraction studies reveal a structure similar to the predicted paired structure (*2*). Near 39 GPa, lithium transforms to a cubic polymorph with 16 atoms per unit cell (cI16), a recently discovered structure unique to lithium (*2*). Additionally, a minimum in the electronic density of states close to the Fermi energy suggests near-insulator behavior in the paired structure.

The ambient-pressure phase of Li at low temperature is not bcc but rather a closed packed rhombohedral 9R structure (*3*). Under ambient pressure, no sign of superconductivity in lithium has been detected down to 4 mK (*4*). However, it is predicted that lithium's structural changes under pressure may have large effects on possible superconductivity in the material (*1*, *5*). Explicit calculations (*6*) suggest that T_c may reach a maximum of 60 to 80 K in the cI16 phase. An early resistivity experiment had indicated a possible superconducting transition in lithium (*7*) at 7 K and higher pressures; however, the experiment was inconclusive due to the lack of magnetic signature of the transition. Similar experiments, performed recently with a diamond anvil cell to higher pressures, confirmed a resistance drop and established a dependence of the drop on external magnetic field but still lacked the magnetic susceptibility measurement necessary for proving superconductivity (*8*). Because of the difficulties in studying the material under pressure [e.g., sample containment and reactivity (*2*, *9*)], it is essential to apply a variety of probes of the compressed sample. For superconductivity, this includes the combination of magnetic (*10*) and electrical (*11*) techniques.

Magnetic susceptibility measurements were performed in two experiments (*12*). The temperature scan at 28 GPa in the second run is shown in Fig. 1. We used a Nb sample placed in the compensating coil at ambient pressure as a reference in this experiment. The signal from Nb is superimposed in phase with the background; the signal from Li is opposite in phase from that of the background. The compensating and signal coils are connected in opposition; thus, the signal from Li has actually the same phase as that from Nb and, therefore, indubitably corresponds to the superconducting transition. We observed

[1]Geophysical Laboratory, Carnegie Institution of Washington, 5251 Broad Branch Road, N.W., Washington, DC 20015, USA. [2]Max Planck Institut für Chemie, Postfach 3060, 55020 Mainz, Germany. [3]Thomas S. Wootton High School, Rockville, MD 20850, USA.

*To whom correspondence should be addressed. E-mail: struzhkin@gl.ciw.edu